22. Swift, J. H., Aagaard, K. & Malmberg, S.-A. The contribution of the Denmark Strait overflow to the deep North Atlantic. *Deep-Sea Res.* **27**, 29–42 (1980).
23. Mauritzen, C. Production of dense overflow waters feeding the North Atlantic across the Greenland–Scotland ridge. Part 1: Evidence for a revised circulation scheme. *Deep-Sea Res. I* **43**, 769–806 (1996).
24. Strass, V. H., Fahrbach, E., Schauer, U. & Sellman, L. Formation of Denmark Strait Overflow water by mixing in the East Greenland Current. *J. Geophys. Res.* **98**, 6907–6919 (1993).
25. Bönisch, G., Blindheim, J., Bullister, J. L., Schlosser, P. & Wallace, D. W. R. Long-term trends of temperature, salinity, density and transient tracers in the central Greenland Sea. *J. Geophys. Res.* **102**, 18553–18571 (1997).
26. Mysak, L. A., Manak, D. K. & Marsden, R. F. Sea-ice anomalies observed in the Greenland and Labrador Seas during 1901–1984 and their relation to an interdecadal Arctic climate cycle. *Clim. Dyn.* **5**, 111–133 (1990).
27. Häkkinen, S. An Arctic source for the Great Salinity Anomaly: a simulation of the Arctic Ice-Ocean system for 1955–75. *J. Geophys. Res.* **98**, 16397–16410 (1993).
28. Dickson, R. R., Meincke, J., Malmberg, S-A. & Lee, A. J. The "Great Salinity Anomaly" in the northern North Atlantic 1968–1982. *Prog. Oceanogr.* **20**, 103–151 (1988).
29. Rahmstorf, S. Rapid climate transitions in a coupled ocean–atmosphere model. *Nature* **372**, 82–85 (1994).
30. Webb, R. S., Rind, D. H., Lehman, S. J., Healy, R. J. & Sigman, D. Influence of ocean heat transport on the climate of the last glacial maximum. *Nature* **385**, 695–699 (1997).

Correspondence and requests for materials should be addressed to the author (e-mail: S.Bacon@soc. soton.ac.uk).

Melt to mush variations in crustal magma properties along the ridge crest at the southern East Pacific Rise

S. C. Singh*, G. M. Kent†, J. S. Collier*, A. J. Harding† & J. A. Orcutt†

* *BIRPS, Bullard Laboratories, University of Cambridge, Cambridge CB3 0EZ, UK*
† *Ida & Cecil Green Institute of Geophysics and Planetary Physics, University of California, San Diego, La Jolla, California 92093, USA*

The determination of along-axis variations in melt properties within the crustal axial magma chamber beneath fast spreading axes is important for understanding melt delivery from the mantle, eruption history along the ridge crest, and the process of crustal accretion. Seismic reflection images[1-4] have shown the molten sill to be continuous along the ridge crest for many tens of kilometres with varying widths (250–4,500 m), but variations in its seismic properties and thickness have remained elusive, despite several attempts to constrain these properties[5-7]. Here we report that the melt sill along the southern East Pacific Rise, which is about 50 m thick, undergoes abrupt changes in its internal properties, ranging from pure melt to mush. The 60-km-long ridge-crest segment near $14°00'$ S is characterized by three 2–4-km sections containing pure melt embedded within a magma chamber rich in mush. These small pure melt pockets may represent a fresh supply of magma from the mantle, capable of erupting and forming the upper crust. Conversely, the 80–90% of the magma chamber which is mushy is unlikely to erupt and may influence the lower-crustal accretion.

Here we use single-ship (conventional) and two-ship multichannel seismic (MCS) reflection data collected during the TERA experiment[2]. The linear ridge segment near $14°$ S was the site of a detailed MCS investigation[8], including a conventional seismic reflection experiment with 13 profiles shot across the rise axis, interconnected by an along-axis profile (SEPR45) running the length of the survey area. The conventional seismic profile (Fig. 1) along the ridge crest (SEPR45) shows a continuous reflection from the axial magma chamber (AMC) along the whole profile. In addition, a wide-aperture profile (WAP58) was collected along-axis to complement the single-ship profiles[9]. The maximum source–receiver offset obtained was ~ 7.4 km, which provided coverage of both refracted and reflected arrivals originating at the AMC and above. The extended aperture and variety of seismic data collected along the $14°$ S segment provides a unique opportunity to study the molten state of the AMC.

Seismic (P- and S-wave) velocities of molten material depend on the seismic velocities of its constituent fluid and crystals, and on the way the crystals are organized[10]. Some laboratory measurements have been made on seismic velocities by melting basalts at atmospheric pressure[11,12]. Although we cannot apply these results directly, they, along with theoretical studies[10], provide some insight into the velocity variations as a function of the fluid content. As the fluid content increases from 0% to 100%, the P-wave velocity decreases from that of hot rock to the velocity of fluid (pure melt). The S-wave velocity also decreases with an increase in melt fraction, but it suddenly drops to zero when the percentage of crystals in the melt is small enough that the crystal aggregates are completely disconnected and are unable to support shear stress. The exact temperature and crystal fraction at which the S-wave velocity drops to zero are not well constrained. However, here we describe a melt, at least seismically, by a near-zero S-wave velocity (<0.5 km s^{-1}), and a mush by a non-zero (>1.5 km s^{-1}).

A preliminary inspection of common mid-point (CMP) gathers from the along-axis WAP58 showed the character of the AMC reflection to vary beneath different sections of the ridge (Fig. 2). At CMP 1625, the AMC is a strong event out to at least 3.2 km range whilst the AMC amplitude at CMP 2488 is weak beyond ~ 2 km range. The amplitude of the theoretical reflection coefficient patterns (Fig. 2) suggest the presence of melt at CMP 2488 and mush at CMP 1625. In addition to the P-wave AMC reflection, we recognise a new phase, a converted shear wave arrival within gather 2488 that we will call $P_{melt}S$. The detection of the converted phase is important as it rules out the possibility that the reduction of the P-wave AMC amplitude at CMP 2488 results from navigational errors. $P_{melt}S$ is not strong in CMP 1625, as predicted from our theoretical calculations for a mushy interface, which show the converted phase to have a low amplitude.

To quantify the internal properties of the melt sill, we apply a full waveform inversion to these two CMP gathers (see Methods). The structure of the AMC is well constrained by waveform inversion (Fig. 3). The inversion results show that the AMC reflection is produced by a thin (50-m) low-velocity layer in which the P-wave velocity drops from 6.0 to 3.4 km s^{-1} in gather 2488, and to 4.0 km s^{-1} in gather 1625. At CMP 2488, we determine the S-wave velocity to be close to zero, while beneath CMP 1625 a non-zero (2.3 km s^{-1}) S-wave velocity in the sill is observed.

From the analysis described above it is clear that the crucial window for discriminating between the two gathers is at $\sim 2–3$ km range: if pure melt were present, the amplitude of the AMC reflection would diminish and undergo a phase change, and the converted phase would be strong. We performed a 2–3 km offset stack of the 60-km along-axis line SEPR45 (Fig. 4c, d) (see Methods). The stack indicated that the bulk of this section was underlain by a magma chamber containing mush, but at three locations, separated by 15–20 km, the sill appears to be melt-rich. We then performed partial P-wave and $P_{melt}S$ stacks for both lines SEPR45 (Fig. 4a) and WAP58 (Fig. 4b) that were shot at different times along the same track. As expected, the stacked $P_{melt}S$ event is strong near gather 2488, but absent near gather 1625. Contrary to this, the partial P-wave stack shows strong P-wave energy in the mush zone and weak or no energy in the pure melt zone. Taken together, these two images provide a powerful tool to map the molten state of a magma chamber. As the amplitude of the whole WAP58 stack between CMP 2750 and 3000 is weak, the lateral extent of the pure melt zone is difficult to determine from this profile alone (Fig. 4b). However, SEPR45 (Fig. 4a) suggests that the lateral extent of the pure melt zone is between 2 and 4 km. We also performed
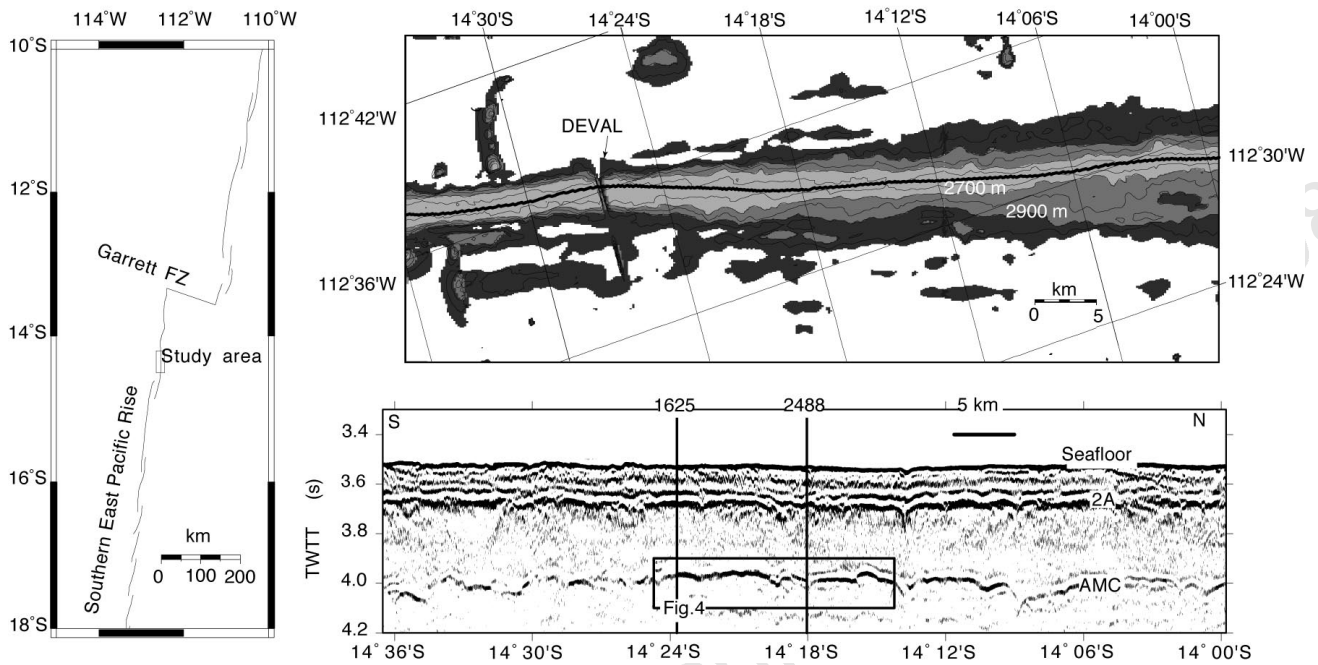
Figure 1 Study area. Left, location map of the study area. Top right, bathymetric map of the southern East Pacific Rise showing location of along-axis profile SEPR45. Bottom right, Conventionally stacked seismic line SEPR 45[8]. The axial magma chamber (AMC) is at ~4 s two-way travel time (TWTT). The locations of CMPs 1625 and 2488 used in the study are also marked.

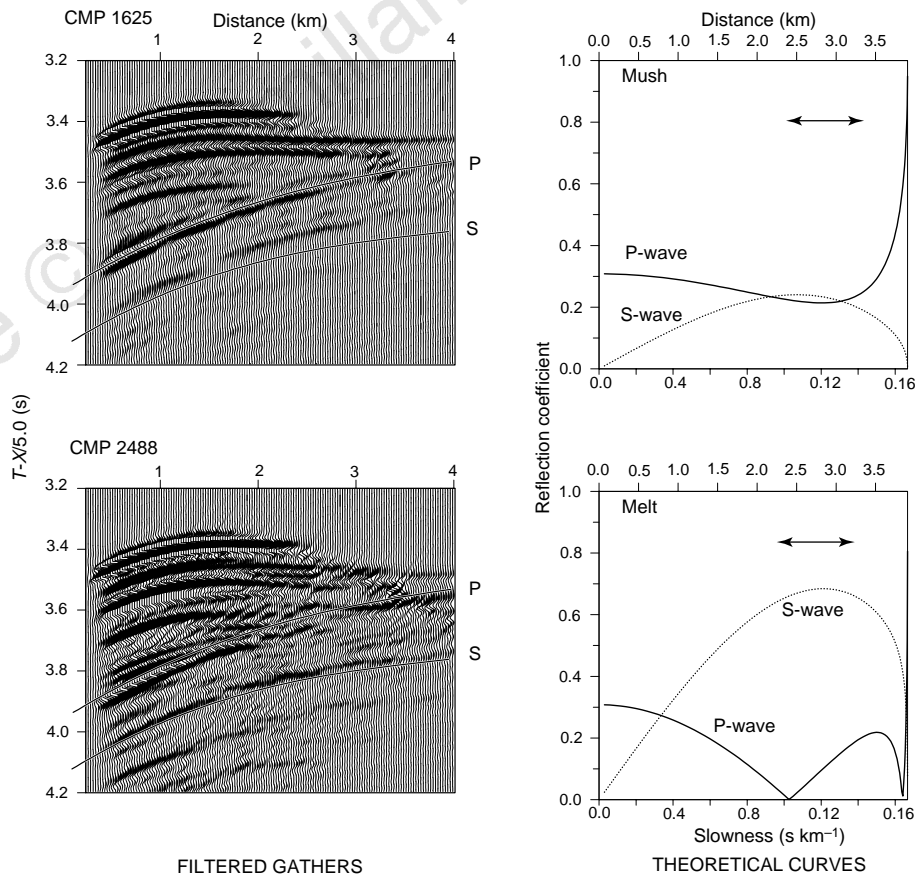FILTERED GATHERS

THEORETICAL CURVES

Figure 2 Common mid-point gathers and theoretical reflection coefficients. Left panels, frequency-wavenumber filtered common mid-point (CMP) gathers from WAP58 (top, CMP 1625; bottom, CMP 2488; see Fig. 1 for location). Travel-time/distance curves for the AMC (P) and $P_{melt}S$ (S) were computed from the P-wave model and Poisson ratio structure from Christeson et al.[24] Right panels, theoretically computed P-wave (solid) and S-wave (dotted) reflection coefficients (displacement) for a P-wave incident at a half-space interface. The upper layer is solid (P-wave velocity $vP = 6.0\,km\,s^{-1}$, S-wave velocity $vS = 3.2\,km\,s^{-1}$, density $= 2,700\,kg\,m^{-3}$) underlain by mush (top panel; $vP = 3.3\,km\,s^{-1}$, $vS = 2.0\,km\,s^{-1}$, density $= 2,600\,kg\,m^{-3}$) and pure melt (bottom panel; $vP = 3.3\,km\,s^{-1}$, $vS = 0.0\,km\,s^{-1}$, density $= 2,600\,kg\,m^{-3}$). We note that a phase reversal occurs beyond the amplitude minimum at ~2.4 km offset in the case of melt. The arrow indicates the distance window used for stacking in Fig. 4.

partial stacks of the across-axis lines in the area, all of which showed the presence of mush. The partial P-wave and S-wave stacks for the most northerly of the three melt locations identified in Fig. 4c were similar to those for the central area, and show that the pure melt zone is ~3 km long. (see Fig. A1 in Supplementary Information) The $P_{melt}S$ stack for the most southerly melt area did not show strong energy.

The P-wave and S-wave velocities obtained from the waveform inversion can be used to constrain the physical state of material within the AMC. The P-wave velocities determined at both locations are slightly higher than expected for pure melt, which could be interpreted as indicating the presence of some crystals in the melt sill. However, the near-zero S-wave velocity at gather 2488 indicates that even if crystals were present they are not connected; thus we suggest that the magma at gather 2488 consists of nearly pure melt. On the other hand, the P-wave velocity at gather 1625 is slightly higher (4.0 km s^{-1}) than observed at gather 2488, but the S-wave velocity is non-zero (2.3 km s^{-1}) suggesting that the crystals are interconnected as they support shear stress. We have defined material with this property within the sill as mush. From theoretical studies[13], one can suggest that 90–95% melt could be present in the pure melt region and 40–60% in the mush zone. On the basis of studies of lava lakes, Marsh[14] argues that a basalt melt with a crystallinity of ~25% behaves rheologically as a solid and it is unlikely to be erupted. This suggestion is consistent with the observation that samples collected at the northern East Pacific Rise tend to contain ~7–10% phenocrysts[15], which implies that there is less likelihood of the mush erupting, whereas the melt lens is capable of erupting.

Over the 60-km seismic section, there seem to be three zones of pure melt, each with 2–4 km of lateral extent (Fig. 4e). The pure melt may correspond to zones of fresh supply of magma from the mantle, and the mush may have gone through a cooling and

crystallization process and hence be more evolved. These lateral variations in magma-chamber structure may inhibit large-scale mixing or flow of magma along the ridge axis. Our analysis also suggests that the AMC could be segmented on a 15–20 km scale, or at least melt may be replenished from the uppermost mantle on a similar length scale (Fig. 4e). Although segmentation in the AMC has been postulated from seismological[16,17], morphological[18] and petrological[19,20] studies, the small-scale melt–mush segmentation is a new result, and provides an insight on the melt delivery, eruption history and crustal accretion along a spreading axis. The presence of 80–90% uneruptable mush in the magma chamber suggests that a large part of the AMC plays a passive role in the crustal accretion, and that the magmatic events such as dyking and eruptions are associated with replenishment of the AMC by magma from a deeper reservoir. This means that the pure melt pockets may be responsible for the upper-crustal formation whereas the mushy zones may influence the accretion of the lower crust. A 2–4-km long, 1,000-m-wide and 50-m-thick pure melt region could cool and crystallize to form mush in a few decades[21], and may explain the temporal variations observed from petrological studies[20]. On a short timescale (a decade or two), the melt supply from the mantle could be episodic[22], filling only the pure melt regions at a scale-length of tens of kilometres along axis. However, on a longer timescale (100–1,000 years), it should be considered a steady-state process where pure melt segments shift along axis to enable a more steady-state style of accretionary emplacement.

Central to obtaining these new results was the determination of the detailed seismic structure of the melt sill at two neighbouring locations, using waveform inversion applied to wide-aperture data. Of equal importance is the identification of a previously unrecognized shear phase that originates at the melt interface, providing additional constraints on the determination of melt sill properties. Quantification of the physical properties could be obtained using
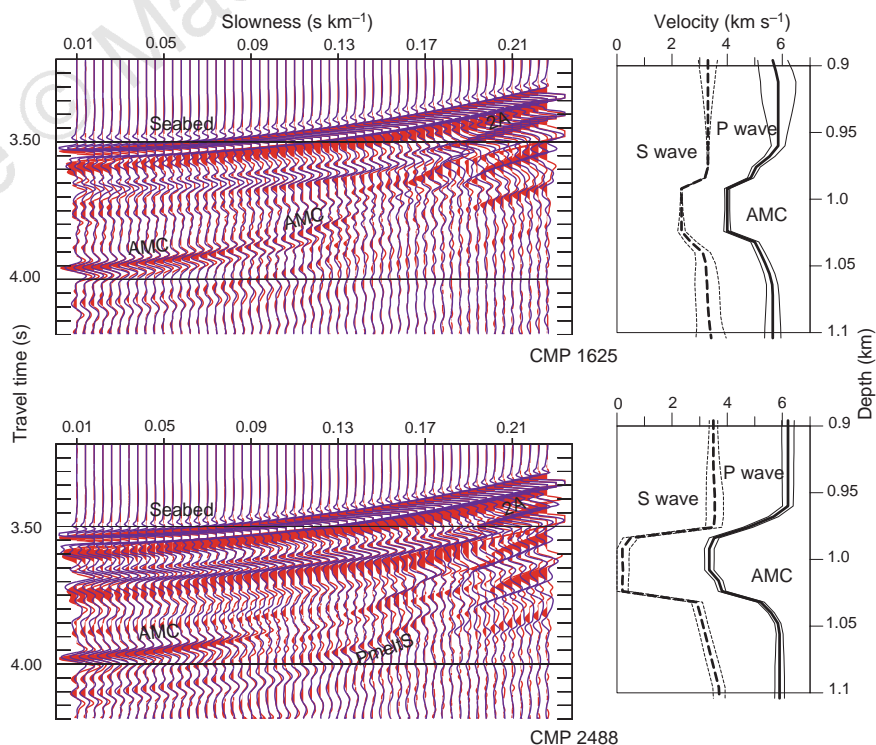

Figure 3 Results of waveform inversion. Left panels, observed (red) and synthetic (blue) data in the tau-slowness domain for WAP58, CMP 1625 (top) and CMP 2488 (bottom). We note the profound difference between the seismic signature of the AMC and the presence of the $P_{melt}S$ phase in CMP 2488. The waveform fit is extremely good within each CMP gather. (For data residuals, see Figs A3 and A4 in Supplementary Information.) Right panels, P-wave and S-wave velocities after

the inversion at CMP 1625 (top) and CMP 2488 (bottom). Thick solid (P-wave) and dashed (S-wave) lines are our best velocity estimates, and thin solid and dashed lines are one standard deviation error in the final velocity models. These errors were estimated from the Hessian matrix[25]. The melt sill is ~50 m thick at the two locations. The S-wave velocity at CMP 2488 is near zero, and is non-zero at CMP 1625.

the waveform inversion technique, which can be thought of as analogous to a borehole sonic log, and in conjunction with $P_{melt}S$ and partial P-wave images it could be used to extend the pinpoint measurements in more continuous fashion. If the properties of the melt in the magma chamber changes with time, our method could be used to determine the temporal variation by analysing data collected over a decadal timescale. More importantly, this technique could be used to predict which melt-rich sections of the ridge crest are likely to erupt next. □

Methods

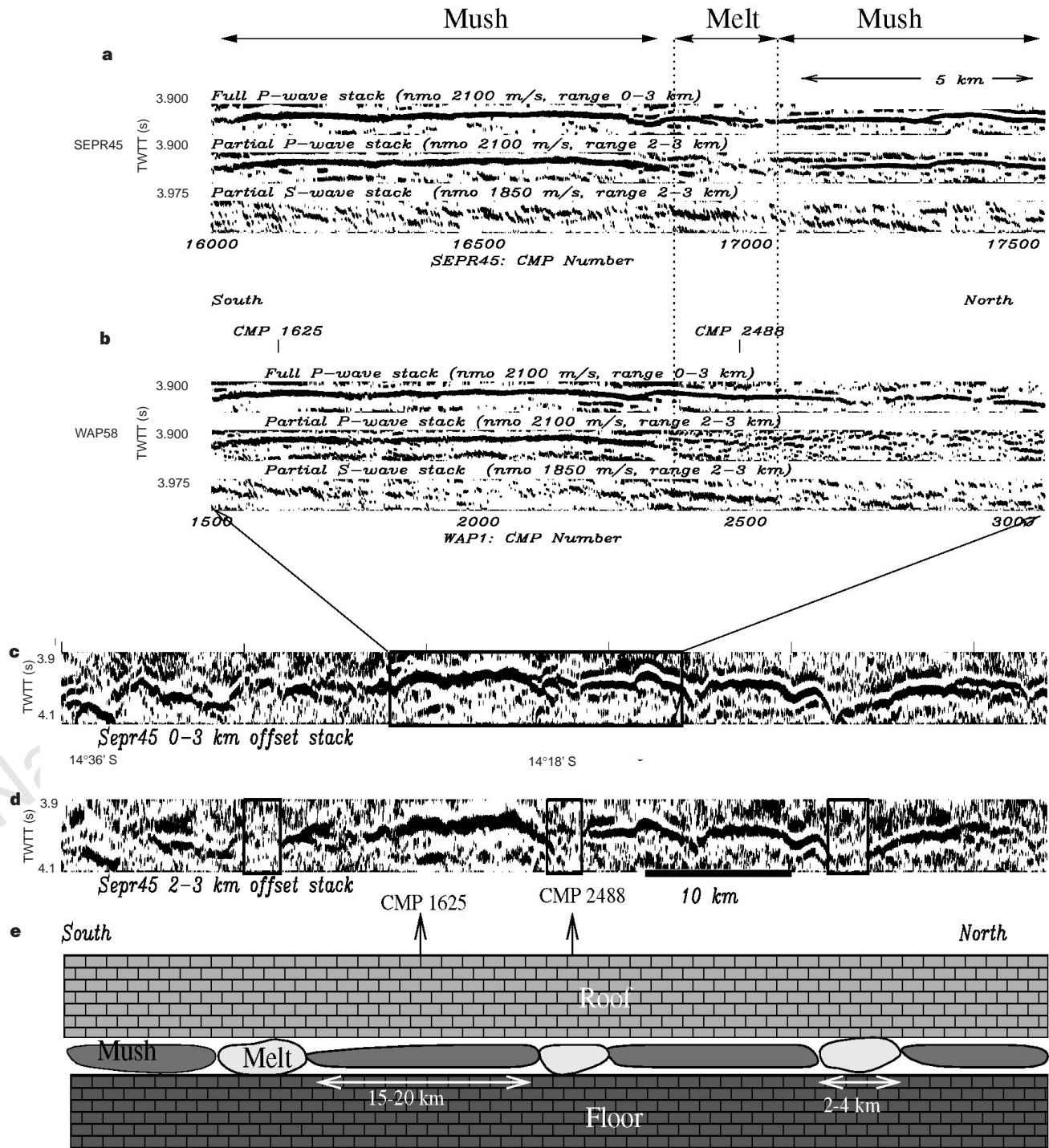**Waveform inversion.** The seismic structure above the magma-chamber

Figure 4 Results of stacking of final interpretation. Full P-wave, partial P-wave and S-wave stack for both SEPR45 (**a**) and WAP58 (**b**), conventional stacked seismic image of SEPR45 of traces in the range 0–3 km offset (**c**). The box in **c** shows the location of the data shown in **a** and **b**. **d**, Partial P-wave stack. The boxes in **d** show the location of lower AMC amplitudes compared to that of the ~0–3 km stack (**c**) suggesting the presence of melt within the chamber. We note the strong AMC image within the 2–3 km offset partial stack **d**, which indicates mush beneath the rest of the section. We interpret the melt zone by the lack of an AMC reflection in the partial P-wave stack, and presence of $P_{melt}S$ in the partial S-wave stack; and vice versa for mush zones **a** and **b**. **e**, Schematic diagram showing the locations of the melt and mush along the ridge axis. (Exact location of the pure melt sections are available; see Fig. A2 in Supplementary Information.)

reflection does not vary significantly along-axis[9], so we use a waveform inversion method that assumes that the layers are horizontally stratified. The inversion scheme is implemented in intercept time-slowness domain[23]. This transformation also allows a clear representation of the AMC and converted arrival ($P_{melt}S$) to be seen (Fig. 3) without interference of slow-phase-velocity events such as the sea-floor reflection. The waveform inversion method determines the P- and S-wave velocities of the crust by improving the fit between observed data and synthetically calculated data. It is an automated method, and therefore reduces human bias and also provides error estimates on the final solution[6,23]. The large-scale initial P-wave velocity was taken from Tolstoy et al.[9]. The initial S-wave velocity was obtained from the P-wave velocity assuming a Poisson's ratio of 0.26 (ref. 24). We used a P-wave attenuation coefficient of 16 for the first 200 m, and 40–90 for the crust below[24]. The S-wave attenuation coefficient was half of the P-wave attenuation coefficient. The model consists of a stack of 8-m-thick layers, for which the P-wave and S-wave velocities, density and attenuation are defined. This sampling interval was based on the minimum thickness that can be resolved from the observed data, which has a frequency bandwidth of 5–30 Hz. As data from all the slownesses were inverted simultaneously, the inverted results contain a model which is consistent with the data from all slownesses, and is therefore less likely to be influenced by incoherent noise due to two- and three-dimensional effects.

The turning rays above the sill and the P-wave reflection arrivals from the AMC constrain the P-wave and S-wave velocities above the AMC. Further constraint on S-wave velocity structure above the AMC comes from the arrival time of the $P_{melt}S$ phase. For this phase, the P-to-S conversion occurs at the solid–fluid interface of the AMC and at the sea bed such that the wave travels one leg between the sea bed and AMC as a P-wave, and the other as an S-wave. The waveforms of the AMC reflection and the $P_{melt}S$ phase constrain P-wave and S-wave velocities within the AMC and its neighbourhood. However, as with all seismic techniques, we have to guard against non-uniqueness of the final solution. To gain confidence in our results, we altered individual features within various candidate models while keeping the rest of the model fixed, and re-ran the inversion; the models that gave the best fit with the data are presented here.

Stacking. To enhance the partial-stack images, we firstly applied a frequency-wavenumber filter to the CMP gathers to remove sea-floor contamination of the AMC events, then performed a normal-moveout correction of 2.10 and 1.85 km s^{-1} for the P-wave and S-wave image, respectively. The partial stacks were obtained by stacking data between 2 and 3 km offsets, and all other processing parameters were as for the ~0–3 km offset stack. We note that the effect of two-dimensional scattering and multiple conversion points for $P_{melt}S$ will tend to provide a minimum estimate of the lateral extent of the pure melt zone. The absence of $P_{melt}S$ stack energy in the melt region could be due to the fact that the $P_{melt}S$ phase has two ray paths with slightly different points of conversion at the AMC that might affect the $P_{melt}S$ stack. Alternatively, the results could be confused by navigational error: that is, the ship track slipping off the axis in this region (Fig. 1).

1. Detrick, R. S. et al. Multi-channel seismic imaging of a crustal magma chamber along the East Pacific Rise. Nature **326,** 35–41 (1987).
2. Detrick, R. S. et al. Seismic structure of the southern East Pacific Rise. Science **259,** 499–503 (1993).
3. Kent, G. M., Harding, A. J. & Orcutt, J. A. Evidence for a smaller magma chamber beneath the East Pacific Rise at 9° 30′ N. Nature **344,** 650–653 (1990).
4. Mutter, J. C. et al. Magma distribution across ridge axis discontinuities on the East Pacific Rise from multi-channel seismic images. Nature **336,** 156–158 (1988).
5. Hussenoeder, S. A. et al. Seismic structure of the axial magma chamber reflector along the southern East Pacific Rise from conventional reflection profiling. J. Geophys. Res. **101,** 22087–22105 (1996).
6. Collier, J. S. & Singh, S. C. Detailed structure of the top of the melt body beneath the East Pacific Rise at 9° 40′ N from waveform inversion of seismic reflection data. J. Geophys. Res. **102,** 20287–20304 (1997).
7. Kent, G. M., Harding, A. J. & Orcutt, J. A. Distribution of magma beneath the East Pacific Rise between the Clipperton transform and the 9° 17′ Deval from forward modelling of common depth point data. J. Geophys. Res. **98,** 13945–13970 (1993).
8. Kent, G. M., Harding, A. J. & Orcutt, J. A. Uniform accretion of oceanic crust south of the Garrett transform at 14° 15′ S on the East Pacific Rise. J. Geophys. Res. **99,** 9097–9116 (1994).
9. Tolstoy, M. et al. Deepening of the axial magma chamber on the southern East Pacific Rise towards the Garrett Fracture Zone. J. Geophys. Res. **102,** 3097–3108 (1997).
10. Schmeling, H. Numerical models on the influence of partial melt on elastic, anelastic and electrical properties of rocks: I Elasticity and anelasticity. Phys. Earth. Planet. Inter. **41,** 34–57 (1985).
11. Murase, T. & McBirney, A. R. Properties of some common igneous rocks and their melts at high temperature. Geol. Soc. Am. Bull. **84,** 3563–3592 (1973).
12. Manghnani, M. H., Sato, H. & Rai, C. S. Ultrasonic velocity and attenuation measurements on basalt melts to 1500 °C: Role of composition and structure in the visco-elastic properties. J. Geophys. Res. **91,** 9333–9342 (1986).
13. Mainprice, D. Modelling the anisotropic seismic properties of partially molten rocks found at mid-ocean ridges. Tectonophysics **279,** 161–179 (1997).
14. Marsh, B. D. Magma chamber. Annu. Rev. Earth Planet. Sci. **17,** 439–474 (1989).
15. Batiza, R. & Niu, Y. Petrology and magma chamber processes at the East Pacific Rise. J. Geophys. Res. **97,** 6779–6797 (1992).
16. Hooft, E. E., Detrick, R. S. & Kent, G. M. Seismic structure and indicators of magma budget along the southern East Pacific Rise. J. Geophys. Res. **102,** 27319–27340 (1997).
17. Collier, J. S. & Sinha, M. C. Seismic mapping of a magma chamber beneath the Valu Fa Ridge, Lau basin. J. Geophys. Res. **97,** 14031–14053 (1992).
18. Macdonald, K. C. et al. A new view of the mid-ocean ridge from the behaviour of ridge-axis discontinuities. Nature **335,** 217–225 (1988).
19. Sinton, J. M. et al. Magmatic process at superfast spreading mid-ocean ridges: Glass compositional variations along the East Pacific Rise 13°–23° S. J. Geophys. Res. **96,** 6133–6155 (1991).
20. Langmuir, C. H., Bender, J. F. & Batiza, R. Petrological and tectonic segmentation of the East Pacific Rise. Nature **322,** 422–429 (1986).
21. Worster, M. G., Huppert, H. E. & Sparks, R. S. Convection and crystallisation in magma cooled from above. Earth Planet. Sci. Lett. **101,** 79–89 (1990).
22. Scott, D. R. & Stevenson, D. J. A self-consistent model of melting, magma migration and buoyancy-driven circulation beneath mid-ocean ridges. J. Geophys. Res. **94,** 2973–2988 (1989).
23. Kormendi, F. & Dietrich, M. Non-linear waveform inversion of plane-wave seismograms in stratified elastic media. Geophysics **56,** 664–674 (1991).
24. Christeson, G. L., Wilcock, W. S. D. & Purdy, G. M. The shallow attenuation structure of the fast-spreading East Pacific Rise near 9° 30′ N. Geophys. Res. Lett. **21,** 321–324 (1994).
25. Tarantola, A. Inverse Problem Theory (Elsevier, New York, 1987).

The intensity of the Earth's magnetic field over the past 160 million years

M. T. Juárez*, **L. Tauxe**†, **J. S. Gee**† & **T. Pick**‡

* Fort Hoofddijk Paleomagnetic Laboratory, Budapestlaan 17, 3584 CD Utrecht, The Netherlands
† Scripps Institution of Oceanography, La Jolla, California 92093-0220, USA
‡ European Topic Center on Catalogue of Data Sources, Archivstrasse 2, D-30169 Hannover, Germany

In contrast to our detailed knowledge of the directional behaviour of the Earth's magnetic field during geological and historical times[1,2], data constraining the past intensity of the field remain relatively scarce. This is mainly due to the difficulty in obtaining reliable palaeointensity measurements, a problem that is intrinsic to the geological materials which record the Earth's magnetic field. Although the palaeointensity database has grown modestly over recent years[3–5], these data are restricted to a few geographical locations and more than one-third of the data record the field over only the past 5 Myr—the most recent database[5] covering the time interval from 5 to 160 Myr contains only about 100 palaeointensity measurements. Here we present 21 new data points from the interval 5–160 Myr obtained from submarine basalt glasses collected from locations throughout the world's oceans. Whereas previous estimates for the average dipole moment were comparable to that of the Earth's present field[6], the new data suggest an average dipole moment of $(4.2 \pm 2.3) \times 10^{22}$ A m^2, or approximately half the present magnetic-field intensity. This lower average value should provide an important constraint for future efforts to model the convective processes in the Earth's core which have been responsible for generating the magnetic field.

To augment the palaeointensity database, we focused on submarine basaltic glass (SBG) obtained from 20 sites sampled by the Deep Sea Drilling Project (DSDP). In addition to the DSDP glasses, we also include results from SBG obtained from pillow lavas in the Troodos ophiolite on Cyprus. SBG has been shown to contain predominantly single-domain magnetite as the carrier of the rema-